AGU PUBLICATIONS

JGR

Journal of Geophysical Research: Solid Earth

RESEARCH ARTICLE
10.1002/2014JB011180

Key Points:
- Cooling magma can be a driving force for volcanic DLP events
- Produced strain rates are ~10^{-13} per s for a characteristic timescale of 100 years
- Correlation between the cluster shapes and focal mechanisms is predicted

Correspondence to:
N. Aso,
aso@eps.s.u-tokyo.ac.jp

Citation:
Aso, N., and V. C. Tsai (2014), Cooling magma model for deep volcanic long-period earthquakes, *J. Geophys. Res. Solid Earth*, *119*, 8442–8456, doi:10.1002/2014JB011180.

Received 8 APR 2014
Accepted 9 OCT 2014
Accepted article online 16 OCT 2014
Published online 28 NOV 2014

Cooling magma model for deep volcanic long-period earthquakes

Naofumi Aso[1] and Victor C. Tsai[2]

[1]Graduate School of Science, University of Tokyo, Tokyo, Japan, [2]Seismological Laboratory, California Institute of Technology, Pasadena, California, USA

Abstract Deep long-period events (DLP events) or deep low-frequency earthquakes (deep LFEs) are deep earthquakes that radiate low-frequency seismic waves. While tectonic deep LFEs on plate boundaries are thought to be slip events, there have only been a limited number of studies on the physical mechanism of volcanic DLP events around the Moho (crust-mantle boundary) beneath volcanoes. One reasonable mechanism capable of producing their initial fractures is the effect of thermal stresses. Since ascending magma diapirs tend to stagnate near the Moho, where the vertical gradient of density is high, we suggest that cooling magma may play an important role in volcanic DLP event occurrence. Assuming an initial thermal perturbation of 400°C within a tabular magma of half width 41 m or a cylindrical magma of 74 m radius, thermal strain rates within the intruded magma are higher than tectonic strain rates of ~ 10^{-14} s^{-1} and produce a total strain of 2×10^{-4}. Shear brittle fractures generated by the thermal strains can produce a compensated linear vector dipole mechanism as observed and potentially also explain the harmonic seismic waveforms from an excited resonance. In our model, we predict correlation between the particular shape of the cluster and the orientation of focal mechanisms, which is partly supported by observations of Aso and Ide (2014). To assess the generality of our cooling magma model as a cause for volcanic DLP events, additional work on relocations and focal mechanisms is essential and would be important to understanding the physical processes causing volcanic DLP events.

1. Introduction

Deep long-period events (DLP events) or deep low-frequency earthquakes (deep LFEs), which are small earthquakes ($M < 2$) occurring at depths of ~10–45 km that radiate low-frequency seismic waves (2–8 Hz), are widely observed worldwide. There are two major types of DLPs: a tectonic type around plate interfaces and a volcanic type beneath volcanoes [*Aso et al.*, 2013]. The tectonic events are often called deep LFEs in seismology [e.g., *Beroza and Ide*, 2011], and the volcanic events are often called DLP events in volcanology [e.g., *McNutt*, 2005]; here we call them deep tectonic LFEs and volcanic DLP events, respectively, to distinguish them from each other. Deep tectonic LFEs have been well studied recently [e.g., *Obara*, 2002; *Rogers and Dragert*, 2003; *Shelly and Hardebeck*, 2010], and they are known to have double-couple mechanisms that suggest slip on the plate interface [*Ide et al.*, 2007; *Frank et al.*, 2013; *Royer and Bostock*, 2013]. In contrast to deep tectonic LFEs, volcanic DLP events also occur near the Moho, but beneath volcanoes worldwide such as in Japan [*Hasegawa and Yamamoto*, 1994], the Aleutians [*Power et al.*, 2004], Cascadia [*Nichols et al.*, 2011], Hawaii [*Aki and Koyanagi*, 1981], the Philippines [*White*, 1996], and Iceland [*Soosalu et al.*, 2010]. Although volcanic DLP events were discovered earlier than tectonic deep LFEs, their physical mechanism has not yet been firmly established. Recently, DLP events or deep LFEs have also been recognized in regions distant from both plate boundaries and active volcanoes [*Aso et al.*, 2011, 2013; *Vidale et al.*, 2014], and *Aso et al.* [2013] inferred that at least some of these events have seismic characteristics similar to those of volcanic DLP events and therefore called them "semivolcanic." In the present study, we treat both volcanic and semivolcanic DLP events collectively as "volcanic DLP events," and provide a model for their physical mechanism.

There are a few observed characteristics that distinguish volcanic DLP events from most other earthquakes. For example, volcanic DLP events often have monochromatic or harmonic waveforms. Their arrivals are emergent, and they tend to have long-duration coda waves [*Power et al.*, 2004]. Another observation is that some volcanic DLP sequences have relatively constant seismicity over 10 year long records [*Aso et al.*, 2011]. Although some volcanic DLP sequences are short-lived sequences occurring before eruptions [*Ukawa and Ohtake*, 1987] and after eruptions [*Power et al.*, 2002], such sequences are thought to be related to the

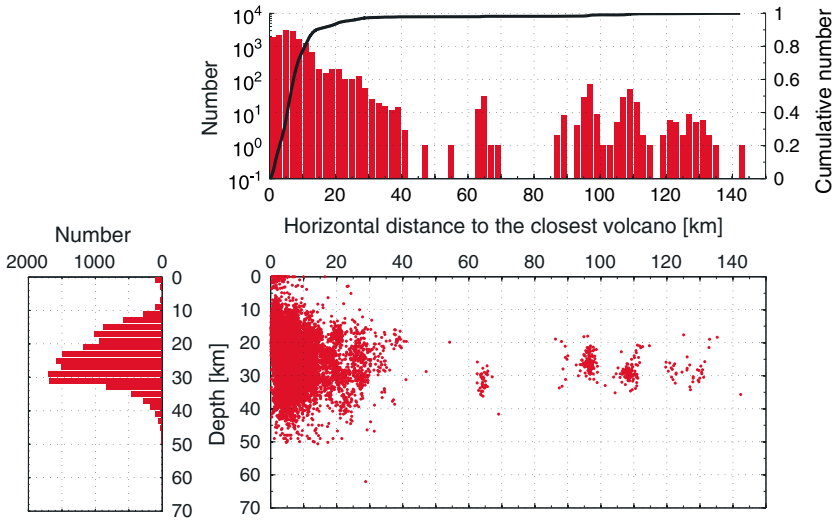

Figure 1. Hypocenter distribution of volcanic DLP events in Japan. (top right) Histogram of volcanic DLP events versus horizontal distance. A black line shows their cumulative number. (bottom right) Depth of volcanic DLP events in Japan versus horizontal distance to the closest volcano. (bottom left) Histogram of volcanic DLP events versus depth.

eruptions, and not commonly observed. On the other hand, many volcanic DLPs also occur beneath dormant volcanoes with relatively constant seismicity (for example, 200–300 events every year in Osaka Bay in western Japan) [*Aso et al*., 2011]. We focus on how to produce such a constant seismicity in the present study. Previous studies have also shown significant non-double-couple amplitudes for volcanic DLP events [e.g., *Nakamichi et al*., 2003; *Aso and Ide*, 2014], with amplitudes instead being consistent with compensated linear vector dipole (CLVD) mechanisms. For example, *Aso and Ide* [2014] obtained CLVD mechanisms for volcanic DLP events in eastern Shimane in western Japan. They also found that these events align in the direction parallel to the CLVD symmetry axis. This correlation between focal mechanisms and source distribution are important constraints on the potential physics involved, and we will use these constraints to motivate our model.

Despite the unique observational constraints on volcanic DLP events, there are few studies on their physical mechanisms. For similar but shallower volcanic long-period events, there have been some studies on physical models such as a resonant oscillation [e.g., *Julian*, 1994; *Kumagai and Chouet*, 2000; *Jellinek and Bercovici*, 2011; *Dmitrieva et al*., 2013], but the majority of this work focuses on the oscillatory nature of seismic waves rather than the initiation mechanism. Here we focus on the latter problem of the generation of initial failure because resonance or other mechanisms typically require an initiation mechanism but such driving forces such as pressure gradients or stress concentrations have not been discussed in the literature. One reasonable mechanism capable of producing such initial forcing, which has been largely ignored so far, is the effect of thermal stresses. To address the question of whether thermal processes in volcanic regions can produce stresses consistent with observed volcanic DLP events, we perform calculations of the thermodynamical stresses within a few simple geometries and their effects on brittle failure. Fluid flow could also be triggered from the same thermal stresses, but even in this case, it is likely that initial brittle failure is necessary, and we therefore focus on the implications of our calculations for such brittle failure.

To further motivate our focus on thermal stresses, we consider the spatial distribution of volcanic DLP events. As shown in Figure 1, most volcanic DLP events occur at depths near the Moho (crust-mantle boundary), and relatively localized to volcanic regions. The localization alone suggests that tectonic forces do not cause these events since tectonic strain would be widespread within the upper plate. On the other hand, since the Moho is a geological discontinuity where the vertical gradient of density is high, it is possible that ascending magma diapirs tend to stagnate there. A stagnant magma body would melt nearby rock just after intrusion and would subsequently cool. This cooling process occurs gradually and probably controls the in situ thermodynamical process for a long time. Therefore, we suggest that cooling magma may play an important role in volcanic DLP event occurrence (Figure 2). Thermal contraction of cooling magma can potentially produce large strain rates and, in the present study, we therefore estimate the thermal strain rates caused by

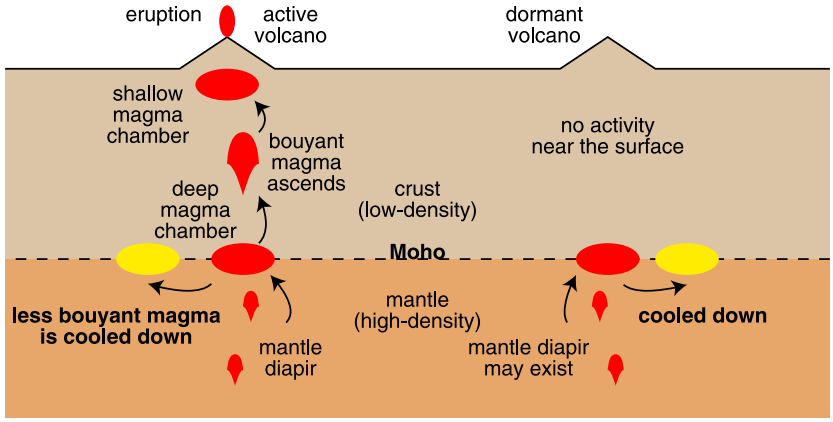

Figure 2. Schematic of magma ascending and cooling for an (left) active volcano scenario and a (right) dormant volcano.

cooling magma near the Moho beneath volcanoes. Then, we verify whether the thermal strain rates can cause brittle failure or not and discuss their connection to the subsequent larger deformations with CLVD mechanisms and low-frequency radiation characteristic of volcanic DLP events. This cooling magma concept is a new idea for the driving force of volcanic DLP events. We note that this model itself does not explain the low-frequency or harmonic characteristics of the seismic waveforms but is an important candidate for their driving force.

2. Model

To model the cooling process of emplaced magma, we set an initial thermal distribution within the intruded magma. We assume simple shapes of magmas because small-scale fluctuations are expected to decay quickly. Typical shapes of magmas are spherical, tabular, and cylindrical, which correspond to three-, two-, and one-dimensional intrusions, but all of them are approximately expressed by finite-length cylinders with various aspect ratios. Therefore, we assume tabular and cylindrical magmas as end-members of magma shapes (Figures 3a and 3b). In section 4.5, we also comment on the results for finite-length cylinders with varying aspect ratios (Figure 3c).

Before providing our calculation, we first comment on the length scales and timescales of interest. Since many volcanic DLP sequences have continuous seismicity over 10 year long records as explained in the section 1, we focus on phenomena whose timescale is longer than 10 years. Since volcanic activity changes over thousands of years, we focus on timescales of 10–1000 years or 3×10^{8}–3×10^{10} s. For a typical thermal diffusivity (10^{-6} m^2/s), the thermal diffusion length scale is 20–200 m over the times considered, although it depends on shape, and is consistent with the width of magma that is inferred from each small cluster of volcanic DLP events reported by *Aso et al.* [2013].

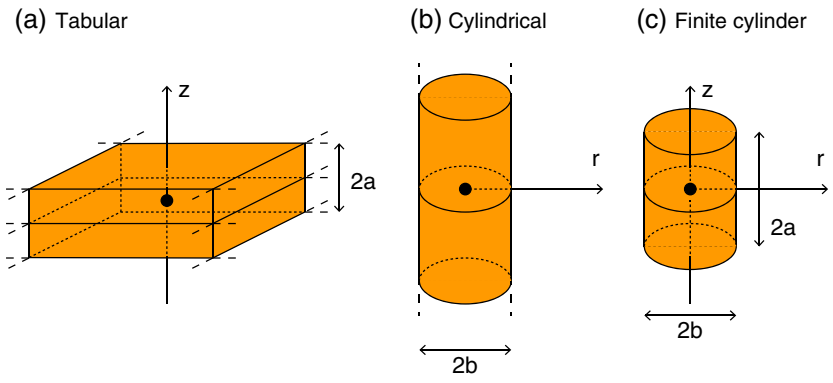

Figure 3. Assumed shapes of intruded magma. The model regions of intruded magma are either (a) tabular, (b) cylindrical and infinitely long, or (c) a finite cylinder.

We assume an initial thermal perturbation of 400°C uniformly throughout the intruded magma. This assumption is appropriate for a near-liquidus body (950–1250°C [*Wyllie*, 1977]) that intrudes into host rock at close to Moho depths (600–800°C [*Yoshioka and Murakami*, 2007]). We do not consider the effect of volatiles because the effect of volatiles is difficult to treat in a simple model and also has large unknowns. For other model parameters, we assume a Poissonian elastic body ($\lambda = \mu$), a thermal diffusivity of $\alpha_0 = 10^{-6}$ m^2 s^{-1}, and a thermal expansion coefficient of $\kappa_0 = 2 \times 10^{-6}$ K^{-1}. To include the effect of partial melting, we assume a density change of $\delta\kappa = 1\%/600$ K$= 1.66 \times 10^{-5}$ K^{-1} so that $\kappa = \kappa_0 + \delta\kappa = 1.86 \times 10^{-5}$ K^{-1} and assume a latent heat release of $\delta c = 400$ kJ kg$^{-1}/600$ K$= 0.66 \times 10^3$ J kg^{-1} K^{-1} so that the specific heat ($c_0 = 10^3$ J kg^{-1} K^{-1}) increases by δc and $\alpha = \alpha_0 c_0/(c_0 + \delta c) = 0.6\alpha_0 = 6 \times 10^{-7}$ m^2 s^{-1}. Although complicated metamorphism might occur, here we adopt a constant rate of partial melting to obtain typical values under homogeneous conditions.

3. Method

In order to achieve our final goal of calculating strain rates throughout the cooling volume, we first calculate the thermal evolution, which can be obtained analytically for the simple geometries assumed. Once the thermal evolution is known, we then calculate the thermal strains. In this section, we separately explain the calculation methods of thermal evolution and thermal strain rates.

3.1. Thermal Calculation

We first calculate the thermal evolution, by solving thermal diffusion equations. We expect convection to be insignificant because Rayleigh numbers can be estimated to be much smaller than the critical Rayleigh number. Detailed derivations are shown in the Appendices A–C. For a tabular intrusion, we set an initial condition of $T = \Delta T$ within $|z| \le a$ and $T = 0$ outside this range. Since the thermal evolution for a thermal perturbation that is expressed as a step function is given by an error function, a plane-symmetric solution is obtained by a combination of error functions as

$$T = \frac{\Delta T}{2}\left[\mathrm{erf}\left(\frac{z^* + a^*}{2\sqrt{t^*}}\right) - \mathrm{erf}\left(\frac{z^* - a^*}{2\sqrt{t^*}}\right)\right] \equiv \Delta T \cdot T_z^*(t^*,\ z^*), \tag{1}$$

where erf(x) is the error function and nondimensional variables are defined as $T^* \equiv T/\Delta T$, $z^* \equiv z/\sqrt{\alpha t_c}$, $a^* \equiv a/\sqrt{\alpha t_c}$, and $t^* \equiv t/t_c$ with a characteristic timescale of t_c.

For a cylindrical intrusion, we set an initial condition of $T = \Delta T$ within $r \le b$ and $T = 0$ outside. Since thermal diffusion in polar coordinates is generally given by a combination of Bessel functions, after Hankel inverse transforming the initial condition, the solution is obtained by a combination of exponential functions about t and Bessel functions about r as

$$T = \Delta T \int_0^\infty J_1(q)\ \exp\left(-\frac{t^*}{b^{*2}}q^2\right) J_0\left(\frac{r^*}{b^*}q\right) \mathrm{d}q \equiv \Delta T \cdot T_r^*(t^*,\ r^*), \tag{2}$$

where $J_n(x)$ is the nth order Bessel function and the nondimensional variables are $r^* \equiv r/\sqrt{\alpha t_c}$ and $b^* \equiv b/\sqrt{\alpha t_c}$.

For a finite-length cylindrical intrusion, separation of variables leads to the solution for an initial condition of $T = \Delta T$ within the region $|z| \le a$ and $r \le b$ and $T = 0$ outside as

$$T = \Delta T \cdot T_z^*(t^*,\ z^*) \cdot T_r^*(t^*,\ r^*), \tag{3}$$

using the solutions (1) and (2) for tabular and cylindrical magmas, respectively, as described above.

We define our characteristic thermal diffusion timescale t_c as the time that it takes for the central temperature perturbation to decrease by half of its original value. This choice of t_c results in $T_z^*(1,\ 0) = T_r^*(1,\ 0) = 0.5$, and normalized diffusion length scales of $a^* = 0.95$ and $b^* = 1.66$. For a realistic value of $t_c = 100$ years, the half width of the tabular intrusion is $a = 41$m and the radius of the cylinder is $b = 74$m.

3.2. Thermal Strain Rates

Thermal strain is produced by a combination of thermal contraction and elasticity. For the case where temperature is driven only by thermal diffusion within a material of homogeneous parameters of elastic constants (λ and μ), volumetric thermal expansion coefficient (κ), and thermal diffusivity (α), and assuming an

adiabatic boundary conditions with no normal displacement, the velocity (v_i) is given as [*Timoshenko and Goodier*, 1970]

$$v_i = \frac{3\lambda + 2\mu}{\lambda + 2\mu}\frac{\alpha\kappa}{3}\frac{\partial T}{\partial x_i}. \tag{4}$$

A detailed derivation is summarized in Appendix D, but the basic reason for this structure is that strain rates are proportional to the time rate of change of temperature, and this time rate of change can be related to spatial temperature gradients through the diffusion equation.

With the thermal evolution obtained in the previous subsection, we calculate the strain rate in cylindrical coordinates as

$$\begin{pmatrix} \dot{\epsilon}_{rr} & \dot{\epsilon}_{r\theta} & \dot{\epsilon}_{rz} \\ \dot{\epsilon}_{\theta r} & \dot{\epsilon}_{\theta\theta} & \dot{\epsilon}_{\theta z} \\ \dot{\epsilon}_{zr} & \dot{\epsilon}_{z\theta} & \dot{\epsilon}_{zz} \end{pmatrix} = \left(\frac{3\lambda + 2\mu}{\lambda + 2\mu}\ \frac{\kappa\Delta T}{3t_c}\right)\begin{pmatrix} \frac{\partial^2 T^*}{\partial r^{*2}} & 0 & \frac{\partial^2 T^*}{\partial r^* \partial z^*} \\ 0 & \frac{1}{r^*}\frac{\partial T^*}{\partial r^*} & 0 \\ \frac{\partial^2 T^*}{\partial r^* \partial z^*} & 0 & \frac{\partial^2 T^*}{\partial z^{*2}} \end{pmatrix} \equiv \left(\frac{3\lambda + 2\mu}{\lambda + 2\mu}\ \frac{\kappa\Delta T}{3t_c}\right)\begin{pmatrix} \dot{\epsilon}^*_{rr} & \dot{\epsilon}^*_{r\theta} & \dot{\epsilon}^*_{rz} \\ \dot{\epsilon}^*_{r\theta} & \dot{\epsilon}^*_{\theta\theta} & \dot{\epsilon}^*_{\theta z} \\ \dot{\epsilon}^*_{rz} & \dot{\epsilon}^*_{\theta z} & \dot{\epsilon}^*_{zz} \end{pmatrix}, \tag{5}$$

where $\dot{\epsilon}^*_{ij}$ is a normalized strain rate. Using its eigenvalues $\dot{\epsilon}^*_1 \geq \dot{\epsilon}^*_2 \geq \dot{\epsilon}^*_3$, we define the differential strain rate as

$$\dot{\epsilon}^*_{\mathrm{dif}} \equiv \frac{\dot{\epsilon}^*_1 - \dot{\epsilon}^*_3}{2}. \tag{6}$$

This value can be used as the intensity of the shear strain rate that we are focusing on, because it is the maximum shear strain rate on microcracks in various directions. High $\dot{\epsilon}^*_{\mathrm{dif}}$ is essential for brittle failure because low strain rates result in ductile relaxation rather than accumulation of elastic strain. In addition, cumulative strains are also important to verify whether shear stresses would be brought above the frictional strength or not. Therefore, we focus on strain rates and cumulative strains in sections 4.2 and 4.3, respectively. In section 4.1, we first examine the thermal evolution model and define the time span of interest.

Isotropic strain can also have an important role in brittle failure because it decreases the effective normal stress on any microcracks. For isotropic strain, one must account for an apparent strain accompanied by density change because it does not produce elastic stress by itself. For example, although cooling material within free space contracts and thermal strain appears, it is accommodated by shortening intermolecular distances, and no elastic stress is produced. This apparent strain is given by

$$\epsilon^*_{\mathrm{app}} \equiv \frac{\kappa}{3}\delta T \Big/ \left(\frac{3\lambda + 2\mu}{\lambda + 2\mu}\frac{\kappa\Delta T}{3}\right) = \frac{\lambda + 2\mu}{3\lambda + 2\mu}\delta T^*, \tag{7}$$

where $\delta T = T - T_0$ and $\delta T^* = \delta T/\Delta T$ are the temperature change and its normalized value. Therefore, the effective isotropic strain is given by

$$\epsilon^*_{\mathrm{iso}} \equiv \frac{1}{3}\sum_i \int \dot{\epsilon}^*_{ii}\, \mathrm{d}t^* - \epsilon^*_{\mathrm{app}} = \frac{\delta T^*}{3} - \frac{\lambda + 2\mu}{3\lambda + 2\mu}\delta T^* = \frac{-4\mu}{3(3\lambda + 2\mu)}\delta T^*. \tag{8}$$

4. Results

4.1. Neglecting Early Stage Deformation

The spatiotemporal distribution of deviatoric strain rates for a tabular intrusion is shown in Figure 4a, and the corresponding result for a cylindrical intrusion is shown in Figure 5a. As shown by both the radii of the beach balls and the contours, the strain rates observed for $t^* < 1.0$ are substantially larger than strain rates at times $t^* > 1.0$, because of the high thermal gradients at early times. However, the temperatures

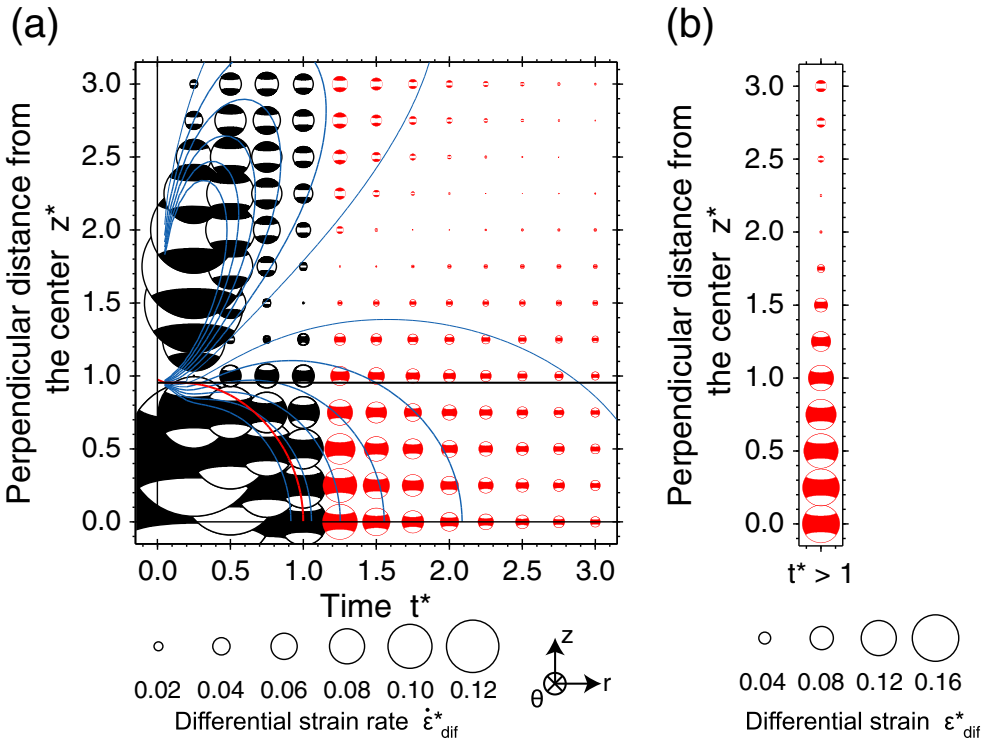

Figure 4. Thermal strain rates and strains for a tabular intrusion. (a) Thermal strain rates and (b) cumulative thermal strains for $t^* > 1$ caused by a tabular intrusion. The spatiotemporal distribution of deviatoric strain rates are shown in Figure 4a. Time is normalized by t_c, which is the time that it takes for the central temperature perturbation to decrease by half of its original value, and the perpendicular distance from the center is normalized by $\sqrt{\alpha t_c}$. The half width of the tabular region is $a^* = 0.95$. At each grid point, deviatoric strain rates are depicted by a beach ball whose diameter corresponds to the differential strain rate shown in the legend below. Thermal strain rates are normalized by $(3\lambda + 2\mu)\kappa\Delta T/3(\lambda + 2\mu)t_c$. Blue contours correspond to the differential strain rates of $\dot{\epsilon}_1^* - \dot{\epsilon}_3^* = 0.02, 0.04, 0.06, 0.08, 0.10$, and 0.12. A red contour corresponds to the points where $T^* = 0.5$. Cumulative thermal strains for $t^* > 1$ are shown in Figure 4b. Thermal strains are normalized by $(3\lambda + 2\mu)\kappa\Delta T/3(\lambda + 2\mu)$.

at these times are also close to the liquidus so that we expect significant ductile flow instead of accumulation of elastic strain. Here we assume complete relaxation of stresses for $T^* > 0.5$ and no ductile deformation for $T^* < 0.5$. Therefore, we focus only on thermal strain rates at times $t^* > 1.0$. Neglecting the deformation in early stages also allows us to consider more complex shapes than the simple tabular or cylindrical ones described above. In particular, small amounts of surface roughness can be neglected because thermal perturbations associated with these short length scales are expected to decay within $t^* < 1.0$.

4.2. Strain Rates

For a tabular intrusion, the differential thermal strain rate within the intruded region ($z^* < a^* = 0.95$) at times $1 < t^* < 2$ is larger than $\dot{\epsilon}_{\mathrm{dif}}^* \sim 0.04$ (Figure 4a), which corresponds to $\dot{\epsilon}_{\mathrm{dif}} \sim 5 \times 10^{-14}$ s^{-1} for $t_c = 100$ years because the normalization factor for strain rates is $\frac{3\lambda+2\mu}{\lambda+2\mu}\frac{\kappa\Delta T}{3t_c} = 1.3 \times 10^{-12}$ s^{-1}. Although the assumption of a Poissonian material might not be realistic for rocks at near-liquidus temperatures, the differential strains are proportional to $\frac{3\lambda+2\mu}{\lambda+2\mu}$ and are therefore insensitive to the Poisson's ratio (results can vary only by a factor of 2). The ductile relaxation timescale is estimated to be $\tau = 2 \times 10^{11}$ s for a rigidity of 5×10^{10} Pa and a viscosity of 10^{22} Pa s, and brittle failure is thought to occur for strain rates larger than $0.01/\tau = 5 \times 10^{-14}$/s [*Webb and Dingwell*, 1990], which is comparable to our estimated strain rates. To calculate the potential effect of thermal strain, we consider the case that all of the thermal strain is accumulated elastically. We note that the estimated value of thermal strain rate is also larger than the strain rates driven by tectonic loading, which is estimated to be 1.3×10^{-14} s^{-1} within the upper plate of thickness 60 km, assuming that the plate convergence rate is ~5 cm/yr and half of the tectonic strain is released by earthquakes at the plate interface, and therefore, thermal strains have an important role in the local stress-strain state. Since thermal strain rates outside the intruded region ($z^* > a^* = 0.95$) are smaller than inside, we focus on the interior region. For a

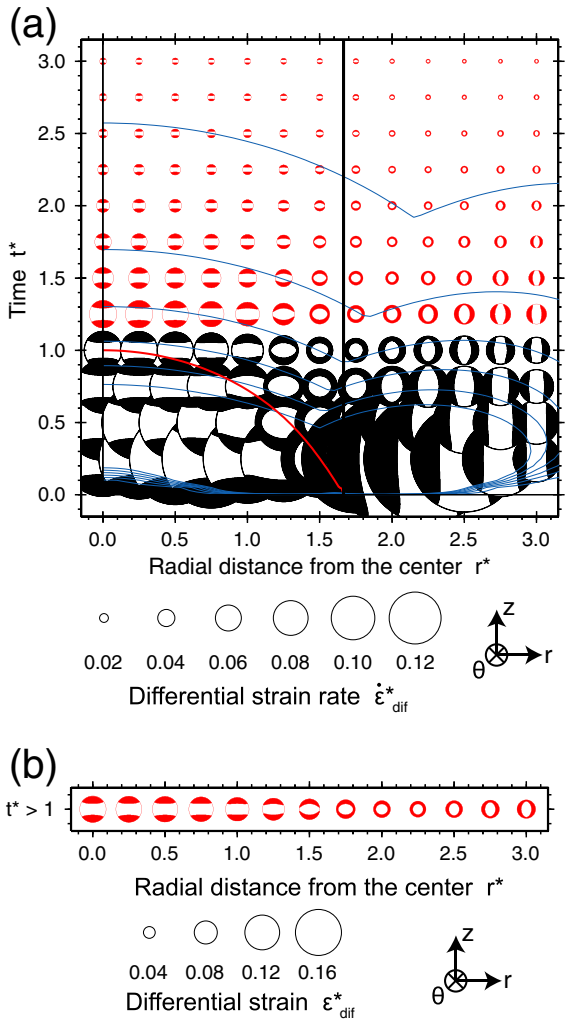

Figure 5. Thermal strain rates and strains for a cylindrical intrusion. (a) Thermal strain rates and (b) cumulative thermal strains of $t^* > 1$ caused by a cylindrical intrusion. Strain rates plotted as in Figure 4a with radial distance from the center axis normalized by $\sqrt{\alpha t_c}$ are shown in Figure 5a. The radius of the cylindrical region is $b^* = 1.66$. Cumulative thermal strains for $t^* > 1$ plotted as in Figure 4b are shown in Figure 5b.

cylindrical intrusion, we obtain similar amplitudes of differential strain rates within the intruded region ($r^* < b^* = 1.66$) at times $1 < t^* < 2$ (Figure 5a).

4.3. Cumulative Strains

For brittle failure, the stress caused by accumulated elastic strain has to reach the frictional strength. Therefore, cumulative strains are as important as strain rates. Here we estimate the cumulative strain and corresponding stress. Cumulative strain over $t^* > 1.0$ is shown in Figures 4b and 5b for the tabular and cylindrical intrusions, respectively. As shown by both the radii of the beach balls and the contours, the cumulative strain within the intruded magma is larger than $\epsilon^*_{dif} \sim 0.1$, which corresponds to $\epsilon_{dif} \sim 4 \times 10^{-4}$ because the normalization factor for strains is $\frac{3\lambda+2\mu}{\lambda+2\mu}\frac{\kappa\Delta T}{3} = 4\times10^{-3}$, for both the tabular and cylindrical intrusions. Corresponding differential stresses are ~12 MPa for a shear modulus of $\mu \sim 30$ GPa and are comparable to the stress drops of many ordinary earthquakes. Differential strains are smaller in the exterior of the intruded magma than in the interior.

It is also of interest to note that despite thermal contraction within the intruded region, the isotropic strain in this region is large and extensional ($\epsilon^*_{iso}/\epsilon^*_{dif} \sim 0.5$) because the contraction is not enough to accommodate the elastic strains produced. Since we focus on the expected initial shear fracture, it is important to consider the Coulomb failure conditions, which account for both normal and shear stresses. This additional isotropic extensional stress brings faults closer to Coulomb failure. In fact, we estimate that these isotropic stresses are as important as shear stresses in reaching the Coulomb threshold.

4.4. Strain Orientations

The orientations of the strain rates for a tabular intrusion are shown in Figure 4a with standard beach ball focal mechanism plots. Here we define the direction of the CLVD axis as the symmetry axis direction, and the polarity of the CLVD as the polarity of the eigenvalue of the deviatoric moment tensor in that direction. Strain rates within the intruded region for the tabular intrusion are negative CLVD in the z direction, because material contracts but it cannot have displacements in the r and θ directions. On the other hand, strain rates within the intruded region for a cylindrical intrusion is positive CLVD (Figure 5a) in the z direction because material contracts but it cannot have displacement in the z direction. The polarity of the CLVD is a notable difference between the tabular and cylindrical intrusions. These same patterns of orientation can also be found for cumulative strain (Figures 4b and 5b).

4.5. Dependency of Shape

We calculated thermal strain rates for tabular and cylindrical magmas, but these shapes are end-members of a finite-length cylinder. To assess the dependency of shape on the thermal strain, we calculated thermal

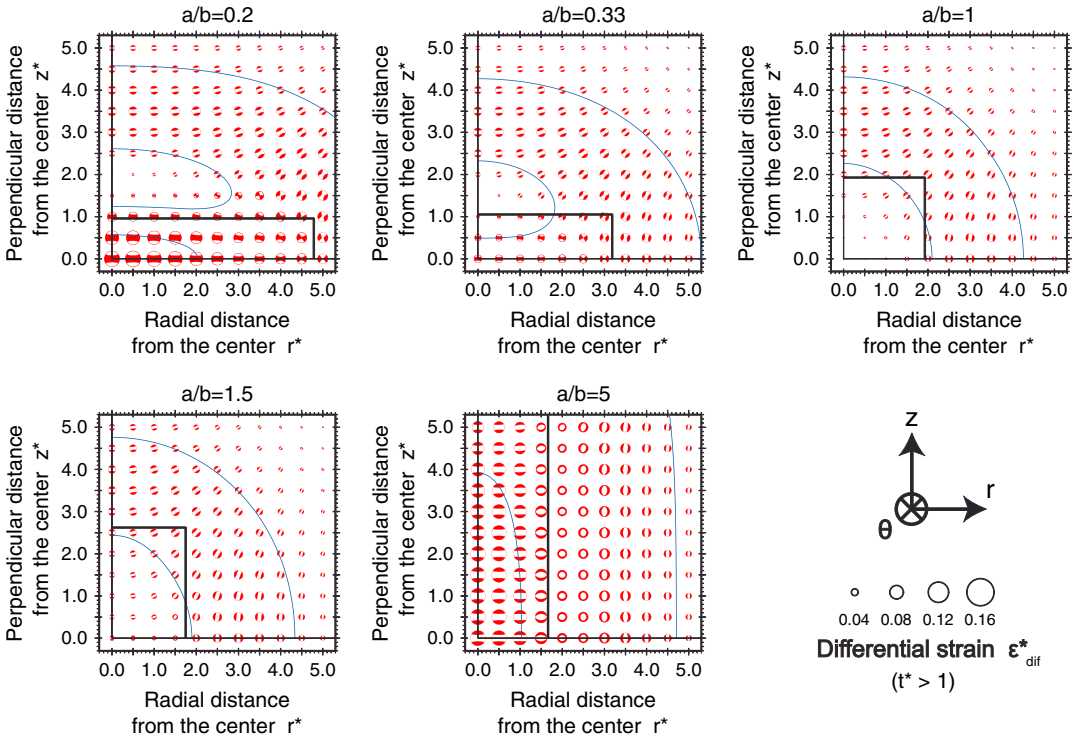

Figure 6. Thermal strains for finite-length cylindrical intrusions. Cumulative thermal strains of $t^* > 1$ are shown for different aspect ratios ($a/b = a^*/b^*$) of finite-length cylinders. Time is normalized by t_c, as before. Black lines represent the intruded regions. In each panel, the vertical axis is the perpendicular distance from the center, and the horizontal axis is the radial distance from the center axis. Distances are normalized by $\sqrt{\alpha t_c}$. Blue contours correspond to differential strains of $\epsilon_1^* - \epsilon_3^* = 0.04,\ 0.08$.

strain for finite cylinders with varying aspect ratios (Figure 6) and compared them with the results for the two simple shapes already analyzed (Figures 4b and 5b). The results for an aspect ratio smaller than 0.2 ($a/b < 0.2$) are close to the results for a tabular intrusion and those for $a/b > 5$ are close to the results for a cylindrical intrusion. We also find that equidimensional intrusions (for which $a/b \sim 1$) do not produce large deviatoric strain rates or cumulative strains.

4.6. Connection to Earthquakes

We expect earthquake focal mechanisms to share the same characteristic orientations as those of the calculated strains. Even if an initial fracture were double couple, a combination of simultaneous double-couple events on faults in various directions that are all consistent with the CLVD-type strain would result in a CLVD mechanism that is similar to the orientation of the thermal strain. Similar observations of CLVD mechanisms composed of multiple double-couple events are also known in shallow volcanic regions [*Ekstrom*, 1994]. Such large deformations could excite a resonance within the intruded region, which could explain the monochromatic or harmonic waveforms often observed for volcanic DLP events. In this manner, the initial shear crack would grow into a finite fault and a resonant oscillation, being affected by the CLVD-type thermal strain. While we do not explicitly model the resonant excitation, the thermally driven process discussed here potentially explains both the CLVD mechanisms and harmonic seismic waveforms, which are the most distinct characteristics observed for volcanic DLP events.

We stress once again that our model itself does not explain the low-frequency or harmonic characteristics of the observed waveforms of volcanic DLP events. These characteristics could come from resonant oscillations or guided waves following the original deformation, but their mechanism is difficult to constrain at this stage. However, in all cases, a driving force is essential for such subsequent phenomena and our model proposes a new possibility for this driving force.

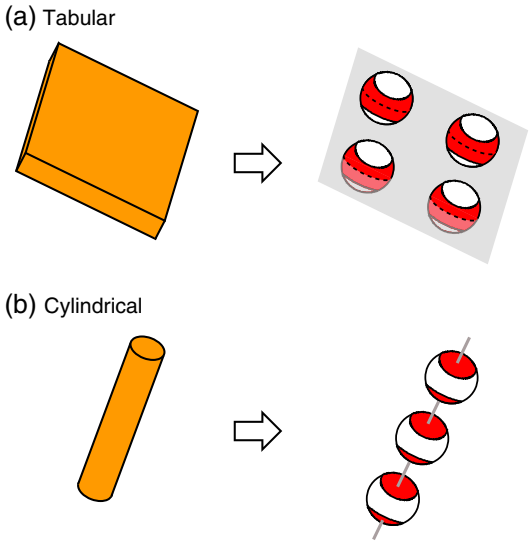

Figure 7. Expected source distribution and focal mechanisms. Schematic illustration of the relationship between the source distribution and focal mechanisms expected from this model for (a) a tabular intrusion and (b) a cylindrical intrusion.

5. Discussion

The thermal strain rates obtained are of the order of 10^{-13} s^{-1} for $t_c = 100$ years, and they contribute to accumulation of elastic strains. This value is larger than the strains from tectonic loading, which are estimated as $\sim 10^{-14}$ s^{-1}, which means that the strain field within the intruded magma is dominated by thermal strain and is dependent on the shape of the magma. Therefore, nearby clusters do not necessarily have similar orientations. This could be one of the reasons why various focal mechanisms are observed even in relatively narrow volcanic regions [*Nakamichi et al*., 2003].

For the models of thermal strain for the tabular and cylindrical intrusions, we obtained a relationship between the shape of intruded magma and the orientation of thermal strain. Assuming that DLP events are distributed within the intruded region and that the focal mechanism orientations are similar to that of thermal strain rates, the focal mechanism is expected to correlate with the particular shape of the cluster. DLP events in a linear cluster would have a positive CLVD mechanism, whose direction is parallel to the orientation of the cluster, and DLP events in a planar cluster would have a negative CLVD mechanism, whose direction is perpendicular to the plane of the cluster (Figure 7). *Aso and Ide* [2014] constrained CLVD mechanisms in the NNE direction for volcanic DLP events within a NNE linear cluster, and this is consistent with our cylindrical model, although it is difficult to determine whether those mechanisms are closer to positive CLVD or negative CLVD because their source is oscillatory. Since a single example is not enough to confirm our model, additional work on mechanism analyses of volcanic DLP events is necessary to verify whether the cooling magma model can drive volcanic DLP events or not.

Since our model itself does not explicitly explain the low-frequency or harmonic characteristics of volcanic DLP events, our model may also be applicable to high-frequency events such as volcano-tectonic events, which are thought to be regular events in volcanic regions. Such high-frequency events sometimes coexist with DLP events [*Shelly and Hill*, 2011], and they may have similar initiation processes. Another possible application of our model could be to shallower events, although the appearance of fluids or volatiles and the resultant convectional heat flow make it unlikely that the simple assumptions made here are appropriate for the shallow crust. The absence of DLP events in the middle crust might be due to the difficulty of having large thermal gradients there.

The process of cooling magma considered here would be a part of a crustal evolution process discussed by *Annen et al*. [2006]. Although it is currently difficult to relate specific aspects of crustal evolution with our cooling magma model, we expect the cooling magma to correspond to the crystallization of mantle-derived basalt or basaltic andesite in the deep crust. If this is correct, the size and shape of these magmas could be inferred from seismological observations with our model, and it may be possible in future work to eventually compare them with geological outcrops and geochemical measurements or to use them to infer the location where andesite emplacements are taking place.

6. Summary

In this work, we have evaluated the strain rates produced by cooling magma in source regions of volcanic DLP events and shown that the thermal strain rates within the intruded magma are so high that they contribute to accumulation of elastic strains and are higher than tectonic strain rates of $\sim 10^{-14}$ s^{-1} for realistic conditions. For a tabular magma of half width 41 m or a cylindrical magma of 74 m radius, the central temperature decreases

by half at $t = 100$ years, and strain rates more than 5×10^{-14} s^{-1} are accumulated elastically for the next 100 years (t = 100–200 years), producing a total strain of 2×10^{-4}. Shear brittle fractures generated by the thermal strains can produce a CLVD mechanism as observed and potentially also explain the harmonic seismic waveforms from an excited resonance. This cooling magma model is also consistent both with the Moho being a density discontinuity and with the seismological evidence of continuous seismicity for more than 10 years.

In our model, DLP events in a linear cluster would have positive CLVD mechanisms whose directions are parallel to the orientation of the cluster, and DLP events in a planar cluster would have negative CLVD mechanisms whose directions are perpendicular to the plane of the cluster. For the DLP events in eastern Shimane in western Japan, the observed correlation between the particular shape of the cluster and orientation of focal mechanisms supports our model. To verify the predicted correlation and assess the generality of our cooling magma model as a cause for volcanic DLP events, additional work on relocations and focal mechanisms of volcanic DLP events is essential and would be important to understanding the physical process of volcanic DLP events.

Appendix A: Thermal Calculation for a Tabular Intrusion (1-D Cartesian Coordinates)

For an extended tabular intrusion, the geometry can be approximated as one dimensional and we solve the associated thermal diffusion problem

$$\frac{\partial T}{\partial t} = \alpha \frac{\partial^2 T}{\partial z^2} \tag{A1}$$

$$\frac{\partial T}{\partial t}(t,\ 0) = 0 \tag{A2}$$

$$T(0,\ z) = \Delta T[H(z + a) - H(z - a)], \tag{A3}$$

where T is temperature, t is time, z is 1-D coordinate, a is half thickness of the tabular intrusion, ΔT is temperature perturbation, and $H(x)$ is the Heaviside function.

Nondimensionalization of equations (A1)–(A3) with a characteristic thermal diffusion timescale of t_c results in

$$\frac{\partial T^*}{\partial t^*} = \frac{\partial^2 T^*}{\partial z^{*2}} \tag{A4}$$

$$\frac{\partial T^*}{\partial t^*}(t^*,\ 0) = 0 \tag{A5}$$

$$T^*(0,\ z^*) = H(z^* + a^*) - H(z^* - a^*), \tag{A6}$$

where $T^* \equiv T/\Delta T$, $t^* \equiv t/t_c$, $z^* \equiv z/\sqrt{\alpha t_c}$, and $a^* \equiv a/\sqrt{\alpha t_c}$.

The general solution satisfying (A4) and (A5) is

$$T^*(t^*,\ z^*) = \int_{-\infty}^{\infty} A(p) \exp\left(-p^2 t^*\right) \exp\left(ipz^*\right) \mathrm{d}p. \tag{A7}$$

Using a Fourier transformation for the initial conditions,

$$T^*(0,\ z^*) = \int_{-\infty}^{\infty} A(p) \exp\left(ipz^*\right) \mathrm{d}p \tag{A8}$$

results in

$$A(p) = \frac{1}{2\pi} \int_{-\infty}^{\infty} T^*(0,\ z^*) \exp\left(-ipz^*\right) \mathrm{d}z. \tag{A9}$$

For the initial conditions of (A6),

$$A(p) = \frac{\exp\left(ipa^*\right) - \exp\left(-ipa^*\right)}{2\pi ip} \tag{A10}$$

so that

$$T^*(t^*,\ z^*) = \int_{-\infty}^{\infty} \frac{\exp[ip(z^*+a^*)] - \exp[ip(z^*-a^*)]}{2\pi ip} \exp\left(-p^2 t^*\right) \mathrm{d}p$$
$$= \int_{\infty}^{-\infty} \frac{\exp\left[-ip'(z^*+a^*)\right] - \exp\left[-ip'(z^*-a^*)\right]}{-2\pi ip'} \exp\left(-p'^2 t^*\right)(-\mathrm{d}p')$$
$$= -\frac{1}{2\pi i}\int_{-\infty}^{\infty} \frac{\exp(-p^2 t^*)}{p} \exp[-ip(z^*+a^*)]\mathrm{d}p$$
$$+ \frac{1}{2\pi i}\int_{-\infty}^{\infty} \frac{\exp(-p^2 t^*)}{p} \exp[-ip(z^*-a^*)]\mathrm{d}p. \tag{A11}$$

Here the elementary Fourier transforms are

$$\int_{-\infty}^{\infty} \exp\left(-p^2 t^*\right) \exp(-ipz^*)\mathrm{d}p = \sqrt{\frac{\pi}{t^*}} \exp\left(-\frac{z^{*2}}{4t^*}\right) \tag{A12}$$

$$\int_{-\infty}^{\infty} \frac{1}{p} \exp(-ipz^*)\mathrm{d}p = -\pi i \,\mathrm{sgn}(z^*), \tag{A13}$$

where sgn(x) is the sign function, and their convolution is calculated as

$$\int_{-\infty}^{\infty} \frac{\exp(-p^2 t^*)}{p} \exp(-ipz^*)\mathrm{d}p = \frac{-\sqrt{\pi}i}{2\sqrt{t^*}}\int_{-\infty}^{\infty} \exp\left(-\frac{\alpha^2}{4t^*}\right) \mathrm{sgn}(z^*-\alpha)\mathrm{d}\alpha$$
$$= \frac{-\sqrt{\pi}i}{\sqrt{t^*}}\int_0^{z^*} \exp\left(-\frac{\alpha^2}{4t^*}\right)\mathrm{d}\alpha = -2\sqrt{\pi}i\int_0^{\frac{z^*}{2\sqrt{t^*}}} \exp\left(-\beta^2\right)\mathrm{d}\beta = -\pi i \mathrm{erf}\left(\frac{z^*}{2\sqrt{t^*}}\right), \tag{A14}$$

where erf(x) is the error function. Therefore,

$$T^* = \frac{1}{2}\left[\mathrm{erf}\left(\frac{z^*+a^*}{2\sqrt{t^*}}\right) - \mathrm{erf}\left(\frac{z^*-a^*}{2\sqrt{t^*}}\right)\right] \equiv T_z^*. \tag{A15}$$

Appendix B: Thermal Calculation for a Cylindrical Intrusion (1-D Polar Coordinates)

For an infinitely long cylindrical intrusion, the geometry can be approximated as one dimensional in the radial direction and we solve the associated thermal diffusion problem

$$\frac{\partial T}{\partial t} = \alpha\left(\frac{\partial^2}{\partial r^2} + \frac{1}{r}\frac{\partial}{\partial r}\right)T \tag{B1}$$

$$\frac{\partial T}{\partial r}(t,\ 0) = 0 \tag{B2}$$

$$T(0,\ r) = \Delta T[1 - H(r-b)], \tag{B3}$$

where r is radial coordinate, b is radius of the cylindrical intrusion, and other variables are as before.

Nondimensionalization of equations (B1)–(B3) results in

$$\frac{\partial T^*}{\partial t^*} = \left(\frac{\partial^2}{\partial r^{*2}} + \frac{1}{r^*}\frac{\partial}{\partial r^*}\right)T^* \tag{B4}$$

$$\frac{\partial T^*}{\partial r^*}(t^*,\ 0) = 0 \tag{B5}$$

$$T^*(0,\ r^*) = 1 - H(r^* - b^*), \tag{B6}$$

where $r^* \equiv r/\sqrt{\alpha t_c}$ and $b^* \equiv b/\sqrt{\alpha t_c}$.

The general solution satisfying (B4) and (B5) is

$$T_r^*(t^*,\ r^*) = \int_0^\infty B(q)\ \exp\left(-q^2 t^*\right) J_0(qr^*)\mathrm{d}q, \tag{B7}$$

where J_n is nth order Bessel function. Using a Hankel transformation for the initial conditions,

$$T^*(0,\ r^*) = \int_0^\infty B(q)\, J_0(qr^*)\mathrm{d}q \tag{B8}$$

$$B(q) = q\int_0^\infty T^*(0,\ r^*)\ J_0(qr^*) r^* \mathrm{d}r^*. \tag{B9}$$

For the initial conditions of (B6),

$$B(q) = q\int_0^{b^*} J_0(qr^*) r^* \mathrm{d}r^* = \frac{1}{q}\int_0^{qb^*} qr^*\, J_0(qr^*)\mathrm{d}(qr^*) = b^* J_1(qb^*) \tag{B10}$$

$$\begin{aligned} T^*(t^*,\ r^*) &= \int_0^\infty \exp\left(-q^2 t^*\right) J_0(qr^*) J_1(qb^*) b^* \mathrm{d}q \\ &= \int_0^\infty \exp\left(-\frac{t^*}{b^{*2}} q^2\right) J_0\left(\frac{r^*}{b^*} q\right) J_1(q)\mathrm{d}q \equiv T_r^*. \end{aligned} \tag{B11}$$

Appendix C: Thermal Calculation for a Finite-Length Cylindrical Intrusion (2-D Cylindrical Coordinates)

We solve the thermal diffusion equation in a cylindrical coordinate system

$$\frac{\partial T}{\partial t} = \alpha\left(\frac{\partial^2}{\partial z^2} + \frac{\partial^2}{\partial r^2} + \frac{1}{r}\frac{\partial}{\partial r}\right) T \tag{C1}$$

with boundary conditions

$$\frac{\partial T}{\partial z}(t,\ 0,\ r) = 0 \tag{C2}$$

$$\frac{\partial T}{\partial r}(t,\ z,\ 0) = 0 \tag{C3}$$

and an initial condition

$$T(0,\ z,\ r) = \Delta T[H(z+a) - H(z-a)][1 - H(r-b)]. \tag{C4}$$

Nondimensionalization of equations (C1)–(C4) results in

$$\frac{\partial T^*}{\partial t^*} = \left(\frac{\partial^2}{\partial z^{*2}} + \frac{\partial^2}{\partial r^{*2}} + \frac{1}{r^*}\frac{\partial}{\partial r^*}\right) T^* \tag{C5}$$

$$\frac{\partial T^*}{\partial z^*}(t^*,\ 0,\ r^*) = 0 \tag{C6}$$

$$\frac{\partial T^*}{\partial r^*}(t^*,\ z^*,\ 0) = 0 \tag{C7}$$

$$T^*(0,\ z^*,\ r^*) = [H(z^* + a^*) - H(z^* - a^*)][1 - H(r^* - b^*)]. \tag{C8}$$

The general solution satisfying (C5)–(C7) is

$$T^*(t^*,\ z^*,\ r^*) = \int_0^\infty\int_0^\infty C(p,\ q)\ \exp\left[-\left(p^2 + q^2\right)t^*\right] \exp\left(ipz^*\right) J_0(qr^*)\ \mathrm{d}q\mathrm{d}p \tag{C9}$$

and therefore,

$$T^*(0,\ z^*,\ r^*) = \int_{-\infty}^\infty\int_0^\infty C(p,\ q) \exp\left(ipz^*\right) J_0(qr^*)\mathrm{d}q\mathrm{d}p. \tag{C10}$$

Here initial condition (C8) is

$$T^*(0,\ z^*,\ r^*) = T_z^*(0,\ z^*)T_r^*(0,\ r^*)\ = \int_{-\infty}^\infty\int_0^\infty A(p)B(q) \exp\left(ipz^*\right) J_0(qr^*)\mathrm{d}q\mathrm{d}p \tag{C11}$$

and therefore, $C(p, q) = A(p)B(q)$. So that

$$T^*(t^*,\ z^*,\ r^*) = \int_{-\infty}^{\infty} A(p)\ \exp\left(-p^2 t^*\right)\exp\left(ipz^*\right)\mathrm{d}p \int_0^{\infty} B(q)\exp\left(-q^2 t^*\right)J_0(qr^*)\mathrm{d}q$$
$$= T_z^*(t^*, z^*)\times T_r^*(t^*,\ r^*). \tag{C12}$$

Appendix D: Thermal Strain and Thermal Stress

Thermal stress calculation is already summarized by *Timoshenko and Goodier* [1970], but here we verify the detailed derivation of strain rates in cylindrical coordinates. At first, we consider Cartesian coordinates. The stress-strain constitutive law is

$$\sigma_{ij} = 2\mu\epsilon_{ij} + \delta_{ij}\lambda\sum_k \epsilon_{kk} - \delta_{ij}(3\lambda + 2\mu)\frac{\kappa}{3}(T - T_0), \tag{D1}$$

where ϵ_{ij}, σ_{ij}, λ, μ, κ, T, and T_0 are strain, stress, Lame's first parameter, shear modulus, and volumetric thermal expansion coefficient. We set λ, μ, and κ as constant parameters.

We assume that displacement is given by a scalar potential $u_i = \frac{\partial\psi}{\partial x_i}$, and therefore, strain is given by $\epsilon_{ij} = \frac{\partial^2\psi}{\partial x_i \partial x_j}$. Solving the equations of equilibrium $\left(\sum_i \sigma_{ij,\ i} = 0\right)$,

$$(\lambda + 2\mu)\nabla^2\frac{\partial\psi}{\partial x_i} - \frac{(3\lambda + 2\mu)\kappa}{3}\frac{\partial}{\partial x_i}(T - T_0) = 0. \tag{D2}$$

Taking its time derivative and replacing the time derivative of temperature with a spatial derivative for the case when temperature is driven only by thermal diffusion $\frac{\partial T}{\partial t} = \alpha\nabla^2 T$,

$$\nabla^2\left[\frac{\partial\dot{\psi}}{\partial x_i} - \frac{(3\lambda + 2\mu)\alpha\kappa}{3(\lambda + 2\mu)}\frac{\partial T}{\partial x_i}\right] = 0 \tag{D3}$$

$$v_i = \frac{\partial\dot{\psi}}{\partial x_i} = \frac{3\lambda + 2\mu}{\lambda + 2\mu}\frac{\alpha\kappa}{3}\frac{\partial T}{\partial x_i} + F_i(x,\ y,\ z,\ t) \tag{D4}$$

where F_i is a harmonic function. For the case of adiabatic ($\partial T/\partial n = 0$) and free surface ($\partial v_i/\partial n = 0$) conditions on the boundary S (therefore $\partial F_i/\partial \mathrm{n} = 0$ on S), F_i is equal to a constant function. Since $v_i = 0$ and $\partial T/\partial x_i = 0$ at the center, $F_i = 0$, and therefore

$$v_i = \frac{3\lambda + 2\mu}{\lambda + 2\mu}\frac{\alpha\kappa}{3}\frac{\partial T}{\partial x_i}. \tag{D5}$$

Therefore, the strain rate in cylindrical coordinates is given by

$$\begin{aligned}
\dot{\epsilon}_{rr} &= \frac{\partial v_r}{\partial r} = \left(\frac{3\lambda + 2\mu}{\lambda + 2\mu}\frac{\alpha\kappa}{3}\right)\frac{\partial^2 T}{\partial r^2}\\
\dot{\epsilon}_{\theta\theta} &= \frac{1}{r}\frac{\partial v_\theta}{\partial\theta} + \frac{v_r}{r} = \left(\frac{3\lambda + 2\mu}{\lambda + 2\mu}\frac{\alpha\kappa}{3}\right)\frac{1\partial T}{r\,\partial r}\\
\dot{\epsilon}_{zz} &= \frac{\partial v_z}{\partial z} = \left(\frac{3\lambda + 2\mu}{\lambda + 2\mu}\frac{\alpha\kappa}{3}\right)\frac{\partial^2 T}{\partial z^2}\\
\dot{\epsilon}_{r\theta} &= \frac{1}{2}\left(\frac{1}{r}\frac{\partial v_r}{\partial\theta} + \frac{\partial v_\theta}{\partial r} - \frac{v_\theta}{r}\right) = 0\\
\dot{\epsilon}_{rz} &= \frac{1}{2}\left(\frac{\partial v_z}{\partial r} + \frac{\partial v_r}{\partial z}\right) = \left(\frac{3\lambda + 2\mu}{\lambda + 2\mu}\frac{\alpha\kappa}{3}\right)\frac{\partial^2 T}{\partial r\partial z}\\
\dot{\epsilon}_{\theta z} &= \frac{1}{2}\left(\frac{\partial v_\theta}{\partial z} + \frac{1\partial v_z}{r\,\partial\theta}\right) = 0.
\end{aligned} \tag{D6}$$

Appendix E: Spatial Derivatives of the Analytic Solutions

For the calculation of thermal strain rates, we give analytic solutions for the spatial derivatives of temperature. The derivatives are

$$T_z^* = \frac{1}{2}\left[\mathrm{erf}\left(\frac{z^*+a^*}{2\sqrt{t^*}}\right) - \mathrm{erf}\left(\frac{z^*-a^*}{2\sqrt{t^*}}\right)\right] \tag{E1}$$

$$\frac{\partial T_z^*}{\partial z^*} = \frac{1}{2\sqrt{\pi t^*}}\left[\exp\left(-\frac{(z^*+a^*)^2}{4t^*}\right) - \exp\left(-\frac{(z^*-a^*)^2}{4t^*}\right)\right] \tag{E2}$$

$$\frac{\partial^2 T_z^*}{\partial z^{*2}} = \frac{-1}{4\sqrt{\pi}t^{*1.5}}\left[(z^*+a^*)\exp\left(-\frac{(z^*+a^*)^2}{4t^*}\right) - (z^*-a^*)\exp\left(-\frac{(z^*-a^*)^2}{4t^*}\right)\right] \tag{E3}$$

and

$$T_r^* = \int_0^\infty \exp\left(-\frac{t^*}{b^{*2}}p^2\right) J_0\left(\frac{r^*}{b^*}p\right) J_1(p)\mathrm{d}p \tag{E4}$$

$$\frac{\partial T_r^*}{\partial r^*} = -\frac{1}{b^*}\int_0^\infty \exp\left(-\frac{t^*}{b^{*2}}p^2\right) J_1\left(\frac{r^*}{b^*}p\right) J_1(p)\, p\, \mathrm{d}p \tag{E5}$$

$$\frac{\partial^2 T_r^*}{\partial r^{*2}} = -\frac{1}{2b^{*2}}\int_0^\infty \exp\left(-\frac{t^*}{b^{*2}}p^2\right)\left[J_0\left(\frac{r^*}{b^*}p\right) - J_2\left(\frac{r^*}{b^*}p\right)\right] J_1(p)\, p^2\, \mathrm{d}p. \tag{E6}$$

Using the recurrence relation $J_n(x)/x = (J_{n-1}(x) + J_{n+1}(x))/2n$,

$$\begin{aligned}\frac{1}{r^*}\frac{\partial T_r^*}{\partial r^*} &= -\frac{1}{b^{*2}}\int_0^\infty \exp\left(-\frac{t^*}{b^{*2}}p^2\right) J_1\left(\frac{r^*}{b^*}p\right)\left(\frac{r^*}{b^*}p\right)^{-1} J_1(p)\, p^2\, \mathrm{d}p \\ &= -\frac{1}{2b^{*2}}\int_0^\infty \exp\left(-\frac{t^*}{b^{*2}}p^2\right)\left[J_0\left(\frac{r^*}{b^*}p\right) + J_2\left(\frac{r^*}{b^*}p\right)\right] J_1(p)\, p^2\, \mathrm{d}p.\end{aligned} \tag{E7}$$

Acknowledgments

Data related to numerical calculations can be found in the appendices. This work was supported by JSPS (12 J09135). Satoshi Ide and Atsuko Namiki are thanked for discussions throughout this work. Comments from Haruhisa Nakamichi, Mike West, and the Associate Editor helped to improve the manuscript.

References

Aki, K., and R. Koyanagi (1981), Deep volcanic tremor and magma ascent mechanism under Kilauea, Hawaii, *J. Geophys. Res.*, *86*(B8), 7095–7109, doi:10.1029/JB086iB08p07095.

Annen, C., J. D. Blundy, and R. S. J. Sparks (2006), The genesis of intermediate and silicic magmas in deep crustal hot zones, *J. Petrol.*, *47*(3), 505–539, doi:10.1093/petrology/egi084.

Aso, N., and S. Ide (2014), Focal mechanisms of deep low-frequency earthquakes in Eastern Shimane in Western Japan, *J. Geophys. Res. Solid Earth*, *119*, 364–377, doi:10.1002/2013JB010681.

Aso, N., K. Ohta, and S. Ide (2011), Volcanic-like low-frequency earthquakes beneath Osaka Bay in the absence of a volcano, *Geophys. Res. Lett.*, *38*, L08303, doi:10.1029/2011GL046935.

Aso, N., K. Ohta, and S. Ide (2013), Tectonic, volcanic, and semi-volcanic deep low-frequency earthquakes in western Japan, *Tectonophysics*, *600*, 27–40, doi:10.1016/j.tecto.2012.12.015.

Beroza, G. C., and S. Ide (2011), Slow earthquakes and nonvolcanic tremor, *Annu. Rev. Earth Planet. Sci.*, *39*, 271–296, doi:10.1146/annurev-earth-040809-152531.

Dmitrieva, K., A. J. Hotovec-Ellis, S. Prejean, and E. M. Dunham (2013), Frictional-faulting model for harmonic tremor before Redoubt Volcano eruptions, *Nat. Geosci.*, *6*(8), 652–656, doi:10.1038/ngeo1879.

Ekstrom, G. (1994), Anomalous earthquakes on volcano ring-fault structures, *Earth Planet. Sci. Lett.*, *128*(3–4), 707–712, doi:10.1016/0012-821X(94)90184-8.

Frank, W. B., N. M. Shapiro, V. Kostoglodov, A. L. Husker, M. Campillo, J. S. Payero, and G. A. Prieto (2013), Low-frequency earthquakes in the Mexican Sweet Spot, *Geophys. Res. Lett.*, *40*, 2661–2666, doi:10.1002/grl.50561.

Hasegawa, A., and A. Yamamoto (1994), Deep, low-frequency microearthquakes in or around seismic low-velocity zones beneath active volcanoes in northeastern Japan, *Tectonophysics*, *233*(3–4), 233–252, doi:10.1016/0040-1951(94)90243-7.

Ide, S., D. R. Shelly, and G. C. Beroza (2007), Mechanism of deep low frequency earthquakes: Further evidence that deep non-volcanic tremor is generated by shear slip on the plate interface, *Geophys. Res. Lett.*, *34*, L03308, doi:10.1029/2006GL028890.

Jellinek, A. M., and D. Bercovici (2011), Seismic tremors and magma wagging during explosive volcanism, *Nature*, *470*(7335), 522–525, doi:10.1038/nature09828.

Julian, B. R. (1994), Volcanic tremor: Nonlinear excitation by fluid flow, *J. Geophys. Res.*, *99*(B6), 11,859–11,877, doi:10.1029/93JB03129.

Kumagai, H., and B. A. Chouet (2000), Acoustic properties of a crack containing magmatic or hydrothermal fluids, *J. Geophys. Res.*, *105*(B11), 25,493–25,512, doi:10.1029/2000JB900273.

McNutt, S. R. (2005), Volcanic seismology, *Annu. Rev. Earth Planet. Sci.*, *32*, 461–491, doi:10.1146/annurev.earth.33.092203.122459.

Nakamichi, H., H. Hamaguchi, S. Tanaka, S. Ueki, T. Nishimura, and A. Hasegawa (2003), Source mechanisms of deep and intermediate-depth low-frequency earthquakes beneath Iwate volcano, northeastern Japan, *Geophys. J. Int.*, *154*(3), 811–828, doi:10.1046/j.1365-246X.2003.01991.x.

Nichols, M. L., S. D. Malone, S. C. Moran, W. A. Thelen, and J. E. Vidale (2011), Deep long-period earthquakes beneath Washington and Oregon volcanoes, *J. Volcanol. Geotherm. Res.*, *200*(3–4), 116–128, doi:10.1016/j.jvolgeores.2010.12.005.

Obara, K. (2002), Nonvolcanic deep tremor associated with subduction in southwest Japan, *Science*, *296*(5573), 1679–1681, doi:10.1126/science.1070378.

Power, J. A., A. D. Jolly, C. J. Nye, and M. L. Harbin (2002), A conceptual model of the Mount Spurr magmatic system from seismic and geochemical observations of the 1992 Crater Peak eruption sequence, *Bull. Volcanol.*, *64*, 206–218.

Power, J. A., S. D. Stihler, R. A. White, and S. C. Moran (2004), Observations of deep long-period (DLP) seismic events beneath Aleutian arc volcanoes; 1989–2002, *J. Volcanol. Geotherm. Res.*, *138*(3), 243–266, doi:10.1016/j.jvolgeores.2004.07.005.

Rogers, G., and H. Dragert (2003), Episodic tremor and slip on the Cascadia subduction zone: The chatter of silent slip, *Science*, *300*(5627), 1942–1943, doi:10.1126/science.1084783.

Royer, A. A., and M. G. Bostock (2013), A comparative study of low frequency earthquake templates in Northern Cascadia, *Earth Planet. Sci. Lett.*, *402*, 247–256, doi:10.1016/j.epsl.2013.08.040.

Shelly, D. R., and J. L. Hardebeck (2010), Precise tremor source locations and amplitude variations along the lower-crustal central San Andreas Fault, *Geophys. Res. Lett.*, *37*, L14301, doi:10.1029/2010GL043672.

Shelly, D. R., and D. P. Hill (2011), Migrating swarms of brittle-failure earthquakes in the lower crust beneath Mammoth Mountain, California, *Geophys. Res. Lett.*, *38*, L20307, doi:10.1029/2011GL049336.

Soosalu, H., J. Key, R. S. White, C. Knox, P. Einarsson, and S. S. Jakobsdóttir (2010), Lower-crustal earthquakes caused by magma movement beneath Askja volcano on the north Iceland rift, *Bull. Volcanol.*, *72*(1), 55–62, doi:10.1007/s00445-009-0297-3.

Timoshenko, S. P., and J. N. Goodier (1970), *Theory of Elasticity*, 3rd ed., McGraw-Hill, New York.

Ukawa, M., and M. Ohtake (1987), A monochromatic earthquake suggesting deep-seated magmatic activity beneath the Izu-Ooshima Volcano, Japan, *J. Geophys. Res.*, *92*(B12), 12,649–12,663, doi:10.1029/JB092iB12p12649.

Vidale, J. E., D. A. Schmidt, S. D. Malone, A. J. Hotovec-Ellis, S. C. Moran, K. C. Creager, and H. Houston (2014), Deep long-period earthquakes west of the volcanic arc in Oregon: Evidence of serpentine dehydration in the fore-arc mantle wedge, *Geophys. Res. Lett.*, *41*, 370–376, doi:10.1002/2013GL059118.

Webb, S. L., and D. B. Dingwell (1990), Non-Newtonian rheology of igneous melts at high stresses and strain rates: Experimental results for rhyolite, andesite, basalt, and nephelinite, *J. Geophys. Res.*, *95*(B10), 15,695–15,701, doi:10.1029/JB095iB10p15695.

White, R. A. (1996), Precursory deep long-period earthquakes at Mount Pinatubo: Spatio-temporal link to basaltic trigger, in *Fire and Mud: Eruptions and Lahars of Mount Pinatubo, Philippines*, edited by C. G. Newhall and R. S. Punongbayan, pp. 307–328, Univ. of Washington Press, Seattle, Wash.

Wyllie, P. J. (1977), Crustal anatexis: An experimental review, *Tectonophysics*, *43*(1–2), 41–71, doi:10.1016/0040-1951(77)90005-1.

Yoshioka, S., and K. Murakami (2007), Temperature distribution of the upper surface of the subducted Philippine Sea Plate along the Nankai Trough, southwest Japan, from a three-dimensional subduction model: Relation to large interplate and low-frequency earthquakes, *Geophys. J. Int.*, *171*(1), 302–315, doi:10.1111/j.1365-246X.2007.03510.x.